Spontaneous instability in internal solitary-like waves

Chengzhu Xu* and Marek Stastna
Department of Applied Mathematics, University of Waterloo, Waterloo, Ontario N2L 3G1, Canada

David Deepwell
Department of Physics, University of Alberta, Edmonton, Alberta T6G 2R3, Canada

(Received 30 July 2018; published 17 January 2019)

The onset and growth of shear instability in large-amplitude internal solitary-like waves propagating in a quasi-two-layer stratification is studied using high-resolution direct numerical simulations with a spectral collocation method. These waves have a minimum Richardson numbers of approximately 0.08 and a length ratio $L_{\mathrm{Ri}}/L_{\mathrm{wave}}$ between 0.80 and 0.88, where L_{Ri} is the length of high shear region with a local Richardson number $\mathrm{Ri} < 0.25$ and L_{wave} is the half-width of the wave. In the wave with $L_{\mathrm{Ri}}/L_{\mathrm{wave}} \approx 0.88$, the onset of instability occurs spontaneously without interacting with any externally imposed physical noise. When $L_{\mathrm{Ri}}/L_{\mathrm{wave}} \lesssim 0.86$, the onset of instability is limited by viscous effects, so that criteria for the onset also include the Reynolds number of the flow field and the amplitude of the external noise. In the wave with $L_{\mathrm{Ri}}/L_{\mathrm{wave}} \approx 0.85$, the spontaneous instability is possible only when the Reynolds number is sufficiently large, whereas in the wave with $L_{\mathrm{Ri}}/L_{\mathrm{wave}} \approx 0.80$, instability does not grow spontaneously but must be triggered by perturbations of finite amplitude. For instabilities triggered by externally imposed noise, the amplitude of the noise has a crucial influence on their growth, whether such noise is in the form of random perturbations or normal-mode disturbances. On the other hand, the importance of non-normal growth decreases as the length ratio $L_{\mathrm{Ri}}/L_{\mathrm{wave}}$ increases and as the amplitude of perturbations increases. In the wave with $L_{\mathrm{Ri}}/L_{\mathrm{wave}} \approx 0.88$, further perturbing the flow field with sufficiently large perturbations leads to the growth of instability on the upstream side of the wave's crest, a result close to the optimal transient growth, even though the perturbations are in the form of normal-mode disturbances.

DOI: 10.1103/PhysRevFluids.4.014805

I. INTRODUCTION

Internal solitary and solitary-like waves (ISWs) are commonly observed in stably stratified fluids such as the Earth's atmosphere and oceans [1]. Due to the balance between nonlinear steepening and dispersive spreading, these waves may propagate over a long distance without substantially changing form, at least in a constant background environment. Nevertheless, as the waves move through a varying environment, they may change their shape gradually, hence possibly becoming unstable. While the propagation of ISWs provides a means for energy transport over large distances, the breaking of ISWs due to instabilities developed during the wave propagation can result in significant energy dissipation and localized turbulent mixing. In open waters, the onset of shear instability along the pycnocline, which occurs when the wave-induced horizontal velocity shear across the wave crest is sufficiently large, plays a fundamental role in the breaking of ISWs [2–7].

*c2xu@uwaterloo.ca

For inviscid, stratified parallel shear flows, a well-known criterion for determining the linear stability involves the gradient Richardson number Ri, defined by

$$\mathrm{Ri} = \frac{N^2}{(\partial U/\partial z)^2}, \tag{1}$$

where N is the buoyancy frequency and U is the horizontal velocity in the background. It measures the strength of the stratification relative to the velocity shear in a parallel flow. A sufficient condition for the flow to be linearly stable is that the local Richardson number exceeds the critical Richardson number 0.25 throughout the flow [8,9]. However, $\mathrm{Ri} < 0.25$ is a necessary but not sufficient condition for instability.

For ISW-induced current across the wave crest, the onset of shear instability is complicated by the finite horizontal extent of the wave and the fact that the ISW-induced current is not an exact parallel, shear flow. As evident in experimental [3] and numerical [4,5] studies, a much lower Richardson number of approximately 0.1 is required for the onset of instability. Additionally, the length of the unstable region (i.e., the region near the wave crest in which $\mathrm{Ri} < 0.25$) relative to the half-width of the ISW must be greater than 0.86 (or 0.8 [5] for a different stratification) in order for the perturbations to amplify to finite amplitude before leaving the wave.

In numerical studies reported in the literature, the instability is typically triggered by perturbing the flow field with small-scale, finite-amplitude perturbations along the pycnocline upstream of the waves. The source of perturbations can be either numerical noise [4] or externally imposed forcing [5,7]. As a result, the onset of instability is in fact dependent on the properties of the initial perturbations. For example, linear stability analysis based on the Taylor-Goldstein equation suggests that, in order for the initial perturbations to develop into instabilities, the temporal growth rate, when multiplied by the time taken by a disturbance to propagate through the unstable region, must exceed 5 [2–4], while the spatial growth rate, when multiplied by the length of the unstable region, must exceed 4 [5]. However, as we pointed out earlier, an ISW-induced current across the wave crest is not necessarily a horizontal parallel flow, and thus the stability predicted by the Taylor-Goldstein equation, which assumes a horizontal parallel flow in derivation, may not be accurate. More recently, Passaggia *et al.* [7] investigated the transient growth of instabilities that originated from the "optimal initial disturbances," which are disturbances that have a maximum growth rate in a given ISW-induced background environment. Such disturbances can maximize their energy growth when passing through the particular ISW-induced background. The authors showed that the optimal disturbances induce a much larger growth rate compared to disturbances based on normal-mode theory, such that the onset of instability is possible in ISWs that are stable to normal-mode disturbances.

Regardless of the methods used for triggering the instability in ISWs, spontaneously generated instability has not been documented in the past literature. In the current paper, we will demonstrate that, for certain ISWs, the onset of spontaneous instability is in fact possible. We will further show that the onset of instability depends not only on the Richardson number-related properties of the waves but also on the Reynolds number of the flow field. For waves in which spontaneous instability does not occur, we will show that the instability can still be triggered by perturbing the initial velocity field. Finally, for waves in which spontaneous instability does occur, we further perturb the flow field with either random perturbations or normal modes. We show that in these cases noise can lead to instabilities that have a much larger growth rate, similarly to those found in Passaggia *et al.* [7] by perturbing the ISWs with optimal disturbances.

The remainder of the paper is organized as follows. The problem is formulated in Sec. II. The simulation results are presented in Sec. III, with Sec. III A focusing on the evolution of the spontaneous instability in a particular case, Secs. III B and III C discussing the viscous and diffusive effects on the onset of spontaneous instability, and Secs. III D and III E discussing simulations in which instability is triggered by external perturbations. Finally, Sec. IV concludes the findings of this work.

II. PROBLEM FORMULATION

A. Governing equations and numerical method

We consider a right-handed Cartesian coordinate system in two dimensions, with the origin fixed at the lower left corner of the computational domain. The x axis is directed to the right along the flat bottom, and the z axis points up toward the surface. Along the x axis, we define the upstream direction to be the direction of wave propagation (i.e., right) and the downstream direction to be the reverse direction (i.e., left).

Numerical simulations presented in this paper were carried out using the numerical model described and validated in Subich *et al.* [10]. The governing equations of the model are the incompressible Navier-Stokes equations under the Boussinesq and rigid lid approximations [11], given by

$$\frac{D\mathbf{u}}{Dt} = -\nabla p - \rho g \hat{k} + \nu \nabla^2 \mathbf{u}, \tag{2a}$$

$$\nabla \cdot \mathbf{u} = 0, \tag{2b}$$

$$\frac{D\rho}{Dt} = \kappa \nabla^2 \rho, \tag{2c}$$

where $\mathbf{u} = (u, w)$ is the velocity field, ρ is the density field, p is the pressure field, g is the acceleration due to gravity, ν is the kinematic viscosity, and κ is the molecular diffusivity. As is the common practice under the Boussinesq approximation, the equations are in dimensional form, except that the density ρ and the pressure p are scaled by the reference density ρ_0. The effect of the Earth's rotation is neglected. For all simulations, periodic boundary conditions are used in the horizontal direction, and free-slip boundary conditions (and Neumann condition for density) are used at the top and bottom boundaries.

The model employs a spectral collocation method [12], which yields highly accurate results at moderate grid resolutions. Nevertheless, in the simulations presented here, we employed high resolution in order to ensure that the thin pycnocline and any instabilities developed near it are well resolved. As appropriate for the boundary conditions, the Fourier transform is applied in the x direction, whereas the Fourier sine or cosine transform is applied in the z direction depending on the variable of interest. For time stepping, an adaptive third-order multistep method is used, where viscous and diffusive terms are solved implicitly, and pressure is computed via operator splitting.

B. Model setup and initialization

We consider a channel of length $L = 4$ m and depth $H = 0.2$ m with a flat bottom and focus on flows in a quasi-two-layer stratification with a dimensionless density difference $\Delta\rho = 0.01$, for which the Boussinesq approximation can be safely adopted. The background density profile, scaled by the reference density ρ_0, is given by

$$\bar{\rho}(z) = 1 - 0.5\Delta\rho \tanh\left(\frac{z - z_0}{d}\right), \tag{3}$$

where z_0 is the location of the pycnocline and d is the half-width of the pycnocline. For all simulations, we set $z_0 = 0.18$ m and $d = 0.005$ m. For simplicity, we do not consider the effect of a background current.

Each simulation is initialized with a single mode-1 ISW, computed by solving the nonlinear eigenvalue problem known as the Dubreil-Jacotin-Long (DJL) equation [13,14]. Without the presence of a background current, the flow is stationary in a reference frame moving with the wave, and the DJL equation takes the form

$$\nabla^2 \eta + \frac{N^2(z - \eta)}{c^2} \eta = 0, \tag{4}$$

TABLE I. Parameters of ISWs. Here, L_{wave} is the half-width of the wave measured according to the formula $L_{\text{wave}} = x_R - x_L$, where x_R and x_L satisfy the equation $u_{\text{top}}(x_R) = u_{\text{top}}(x_L) = 0.5u_{\max}$ with u_{top} being the horizontal velocity profile along the inviscid top boundary, and L_{Ri} is the length of the unstable region in which $\text{Ri} < 0.25$.

Wave	$\lvert\eta\rvert_{\max}$ (m)	c (m/s)	$u_{\max}$ (m/s)	$u_{\min}$ (m/s)	L_{wave} (m)	$\text{Ri}_{\min}$	L_{Ri} (m)	$L_{\text{Ri}}/L_{\text{wave}}$
Small	0.0812	0.0680	0.0612	−0.0569	0.93	0.085	0.75	0.801
Medium	0.0826	0.0680	0.0614	−0.0582	1.23	0.083	1.04	0.851
Large	0.0837	0.0680	0.0614	−0.0594	1.51	0.082	1.33	0.884

with the boundary conditions $\eta(x, 0) = \eta(x, H) = 0$ and $\eta(x, z) \to 0$ as $x \to \pm\infty$. In this equation, $\eta(x, z)$ is the vertical displacement of the isopycnal relative to its far-upstream location, c is the nonlinear wave propagation speed, and N^2 is the square of the buoyancy frequency defined by

$$N^2(z) = -g\frac{d\bar{\rho}}{dz}. \tag{5}$$

The DJL equation is equivalent to the full set of stratified Euler equations in a reference frame moving with the wave, where no assumption with respect to the nonlinearity of fluid flow is made. Hence, solutions of the DJL equation are exact solitary wave solutions in the inviscid limit. For large-amplitude waves, these solutions have been shown to be different from wave forms predicted by weakly nonlinear theories, such as the Korteweg–de Vries (KdV) equation [15,16]. In particular, solutions to the KdV equation have a much smaller horizontal length scale compared to the solutions of the DJL equation, along with a different vertical structure, especially for the vertical profile of shear. Were solutions of the KdV equation used as initial conditions in the simulations reported below, the primary waves would not maintain their initial form on the timescales shown.

The DJL equation is solved numerically using the method described in Dunphy *et al.* [17]. The algorithm is based on the variational scheme developed in Turkington *et al.* [18], which seeks a solution iteratively that minimizes the kinetic energy, subject to the constraint that the available potential energy (APE) is held fixed. The APE measures the amount of potential energy that can be converted into kinetic energy and is specified *a priori* while other wave parameters are determined implicitly by the algorithm. For the stratification used in this work, large-amplitude ISWs are broadening (or conjugate-flow) limited [19]. In this case, the waves may flatten and broaden, while the wave amplitude (measured by the maximum isopycnal displacement $|\eta|_{\max}$), the propagation speed c and the maximum wave-induced horizontal current $u_{\max}$ all approach asymptotic limits with $u_{\max} < c$. The wave-induced flow in the center of such waves is horizontally uniform and is said to be conjugate to the upstream flow.

We consider three broadening limited ISWs, whose parameters are given in Table I. For each wave, the wave's crest is centered at $x = 2$ m initially. With the left and right boundaries located at $x = 0$ and 4 m, respectively, this setup ensures that all components of the wave-induced velocity vanish at the left and right boundaries. In Table I, the gradient Richardson number Ri is defined by

$$\text{Ri} = -\frac{g\rho_z}{u_z^2}, \tag{6}$$

with subscripts denoting partial derivatives. Based on the analysis of Bogucki and Garrett [20], the Richardson number in ISWs is determined by the layer thickness, the pycnocline thickness, and the wave amplitude. By fixing the layer thickness (determined by z_0) and the pycnocline thickness d and having similar wave amplitudes, we are able to obtain a minimum Richardson number that is approximately the same for all waves. This value, $\text{Ri}_{\min} \approx 0.08$, is significantly smaller than the critical Richardson number 0.25 and is also smaller than 0.1 that is required for the presence of shear instability in ISWs [5] (though Passaggia *et al.* [7] suggests that it is not a hard limit). Additionally,

TABLE II. List of simulations. In the case labels, the leading letter indicates the wave being examined, and the letter "P" ("F") indicates that the noise is in the form of random perturbations (normal modes). Cases with "F" have a different setup and will be discussed in Sec. III E.

Simulation	ν (10^{-6} m^2/s)	κ (10^{-7} m^2/s)	Re (10^3)	Re$_S$ (10^2)	Re$_B$	Sc	ϵ (m/s or m)	$N_x \times N_z$	Billow formation
Simulations performed with the *small* ISW									
SR5	1	2	4.97	3.06	12.4	5	0	4096×256	No
SR10	0.5	1	9.94	6.12	24.8	5	0	4096×256	No
SR5P-4	1	2	4.97	3.06	12.4	5	1×10^{-4}	4096×512	Yes
SR5P-3	1	2	4.97	3.06	12.4	5	1×10^{-3}	4096×512	Yes
SR5F-3	1	2	4.97	3.06	12.4	5	2×10^{-3}	8192×512	No
Simulations performed with the *medium* ISW									
MR5	1	2	5.07	3.07	12.7	5	0	4096×256	No
MR10	0.5	1	10.14	6.14	25.4	5	0	4096×512	Yes
Simulations performed with the *large* ISW									
LR5	1	2	5.14	3.07	12.8	5	0	4096×256	Yes
LR10	0.5	1	10.28	6.14	25.7	5	0	4096×512	Yes
LR5S1	1	10	5.14	3.07	12.8	1	0	4096×256	Yes
LR5S20	1	0.5	5.14	3.07	12.8	20	0	8192×512	Yes
LR5P-4	1	2	5.14	3.07	12.8	5	1×10^{-4}	4096×512	Yes
LR25P-4	0.2	0.4	25.70	15.35	64.2	5	1×10^{-4}	8192×1024	Yes
LR5P-3	1	2	5.14	3.07	12.8	5	1×10^{-3}	4096×512	Yes
LR5F-4	1	2	5.14	3.07	12.8	5	5×10^{-4}	8192×512	No[a]
LR5F-3	1	2	5.14	3.07	12.8	5	1×10^{-3}	8192×512	Yes

[a]No billow formation on interaction with normal modes, though billows are formed initially as a result of the spontaneous instability.

the ratio $L_{\mathrm{Ri}}/L_{\mathrm{wave}}$ of the three waves ranges from 0.80 to 0.88, which contains the threshold of $L_{\mathrm{Ri}}/L_{\mathrm{wave}} = 0.86$ determined in Fructus *et al.* [3] and Barad and Fringer [4].

C. Parameter space

Table II gives a list of the simulations discussed in this paper. For the majority of cases, the DJL equation is solved on a coarse grid of size 512×256 (in the x and z directions, respectively), and the solution is then interpolated onto a finer computational grid of size (at least) $N_x \times N_z = 4096 \times 256$ using the cubic interpolation method. This computational grid gives a horizontal and vertical grid spacing of (at most) 9.7×10^{-4} m and 7.8×10^{-4} m, respectively. Most of these simulations are studied in two dimensions, except for the case "LR5" for which three-dimensional simulation has also been performed. In this simulation, the domain has a width $L_y = 0.1$ m, with periodic boundary conditions applied in the spanwise direction. The grid size in the spanwise direction is $N_y = 256$, which gives a grid spacing of 3.9×10^{-4} m.

While ISWs obtained by solving the DJL equation are inviscid phenomena, in our simulations viscous and diffusive effects are not neglected, since the waves studied here are on the laboratory scale. For computational efficiency, however, the free-slip boundary conditions are used at the top and bottom boundaries. This is because for a model that is spectral in all directions, as our model is, the adoption of no-slip conditions requires the Chebyshev discretization [12] in the vertical direction. While this is helpful in resolving the thin boundary layers, it clusters points near the top and bottom boundaries and thus significantly reduces the size of possible time steps. Instead, the free-slip conditions allow us to discretize the domain into equally spaced grid points in the vertical direction by using the Fourier sine or cosine transforms. These equally spaced grid points give a relatively higher resolution at the center of the water column, where significant stratification and velocity shear is present. In fact, cases with no-slip conditions have been tested but no differences in terms of instability onset and instability characteristics were observed. The choice of free slip boundaries would have to be revisited were the topic of interest to be the onset of shear instability in ISWs that are breaking limited [21,22].

We note that there are a variety of Reynolds number definitions available in the literature. Here, we choose to present three of them in Table II. The first one, Re, is defined by

$$\mathrm{Re} = \frac{|\eta|_{\max} u_{\max}}{\nu}, \tag{7}$$

which is relevant to the length and velocity scales set by the ISWs. The second one, Re_S, is the shear Reynolds number, defined in terms of the shear layer thickness by

$$\mathrm{Re}_S = \frac{d u_{\max}}{\nu}. \tag{8}$$

Literature on the effect of viscosity on shear instability [23,24] suggests that instability growth is slowed by viscosity when $\mathrm{Re}_S < \mathcal{O}(100)$ and prevented entirely when $\mathrm{Re}_S < \mathcal{O}(10)$. While these criteria provide a useful guide for determining instability growth in a parallel shear flow, instability in an ISW-induced flow is a much more complicated phenomenon. In fact, Table II suggests that Re_S does not provide a clear indication of billow formation, implying that for ISW-induced flows relying solely on Re_S could be misleading. In order to relate the shear layer thickness and the instability to the bulk ISW scale, we also introduce the buoyancy Reynolds number, Re_B, which is defined by

$$\mathrm{Re}_B = \mathrm{Re}\,\mathrm{Fr}_h^2, \tag{9}$$

where Fr_h is the Froude number. Following Maffioli and Davidson [25], we take Fr_h as the ratio of relevant vertical scales to horizontal scales for the instability. Based on results described below, we estimate

$$\mathrm{Fr}_h \sim \frac{l_v}{l_h} = \frac{L_{\text{stratification}}}{L_{\text{billow}}} = \frac{0.005}{0.1} = 0.05. \tag{10}$$

While these estimates are analogous to those presented by Maffioli and Davidson [25], the physical situation is quite different, as they studied decaying stratified turbulence while we study the onset of instability. In Sec. III B, we shall show that under certain conditions the onset of instability in ISWs can be limited by the viscous effect, even though a value of $\mathrm{Re}_B \gg 1$ implies that viscous dissipation is unimportant in determining the large-scale dynamics such that the ISWs themselves are not profoundly changed by viscosity.

Also in Table II, the Schmidt (or Prandtl) number Sc is defined by

$$\mathrm{Sc} = \frac{\nu}{\kappa}, \tag{11}$$

which measures the strength of the momentum diffusivity relative to the mass diffusivity. In Sec. III C, we will discuss the effect of varying the Schmidt number on the viscous adjustment of ISWs and the onset of instability.

In Table II, simulations without “P” or “F” in their labels are initialized without external perturbations. Among these cases, the *small* wave is always stable while the *large* wave is always unstable. The *medium* wave is conditionally stable, and the key factor for determining its stability is the Reynolds number. In some simulations (those with the letter “P” in their labels), velocity perturbations in the form of additive white noise are applied to the initial flow field. These perturbations have a small but finite amplitude, measured by ϵ (in meters per second) but have no preferred direction or spatial structure. Table II shows that, with the presence of perturbations, instability can also be triggered in the *small* wave which is otherwise stable. For cases with “F” in their labels, perturbations are in the form of free waves, or normal modes, instead of white noise, and ϵ measures the amplitude of density perturbation (in meters) instead of velocity perturbation.

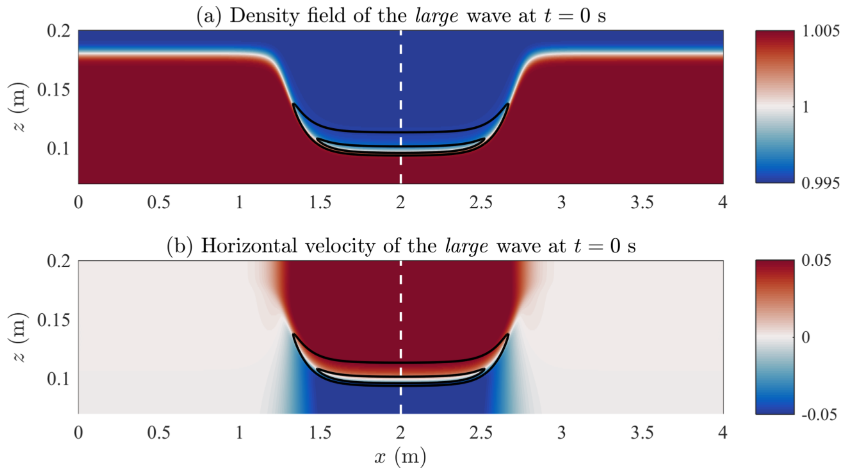

FIG. 1. (a) Density and (b) horizontal velocity fields of the *large* wave at $t = 0$ s. The velocity in (b) is measured in meters per second. The Richardson number contours (black) have values of 0.1 (inside) and 0.25 (outside). The wave's crest is indicated by the dashed lines (white).

These cases have a different setup and will be discussed in detail in Sec. III E. Finally, note that the terms "small," "medium," and "large" are relative, and the amplitude of all waves considered in this work are in fact large relative to the thickness of the upper layer.

D. Stratified shear instability

The classical linear theory suggests that the behavior of perturbations in an inviscid parallel shear flow is governed by the Taylor-Goldstein equation [11], which reads as

$$\frac{d^2\phi}{dz^2} + \left[\frac{N^2(z)}{(c_p - U)^2} + \frac{d^2U/dz^2}{c_p - U} - k^2\right]\phi = 0, \tag{12}$$

with the boundary conditions $\phi(0) = \phi(H) = 0$. In this equation, $U(z)$ is the background horizontal velocity (i.e., the ISW-induced horizontal velocity across the wave's crest in our simulations), k is the wave number of disturbances, and c_p is the (complex) phase speed of disturbances. The eigenfunction $\phi(z)$ characterizes the vertical structure of the velocity field (e.g., the wave-induced horizontal velocity is proportional to $d\phi/dz$). The stability of the flow is determined by c_p such that if the imaginary part of c_p is nonzero, then any finite-amplitude disturbances will grow exponentially with respect to time, until the nonlinear effect becomes dominant. This leads to the onset of shear instability in a stratified parallel shear flow. The Richardson number criterion states that if $\mathrm{Ri} > 0.25$ throughout the flow, then the imaginary part of c_p is guaranteed to be zero [8,9]. The converse is not necessarily true, however. That is, $\mathrm{Ri} < 0.25$ does not necessarily indicate the onset of instability. Also, note that the linear stability theory discussed here describes an idealized situation and thus provides only a rough guide for phenomena observed in this work. It does not preclude the existence of other mechanisms (e.g., non-normal growth [7]) that may trigger the instability in a more complicated situation (e.g., ISW-induced current).

III. SIMULATION RESULTS

A. Base case

We shall first consider the case labeled as "LR5" in Table II, which will be referred to as the "base case" hereafter. The initial density and horizontal velocity fields of this case are plotted in Fig. 1. The Richardson number contours shown in this figure suggest that the local Richardson number is

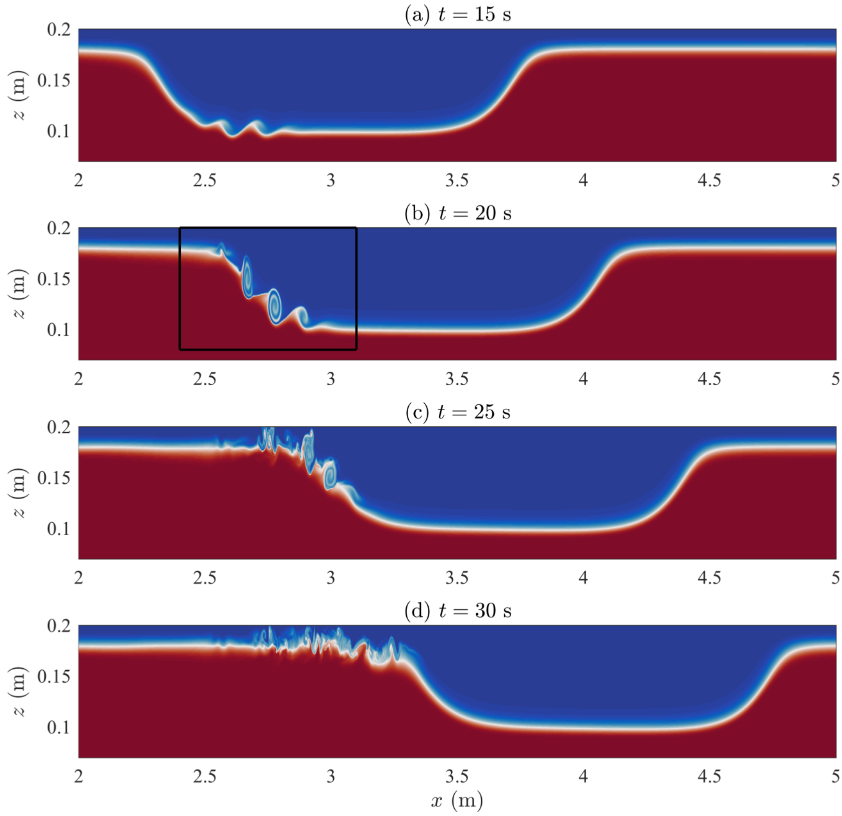

FIG. 2. Shaded density contours showing the evolution of shear instability in the base case at four different times. Detail of the billows in (b) is shown in Fig. 3.

significantly less than 0.25 and even 0.1 over the entire wave crest, creating a region that is highly susceptible to instability. Away from this region, ρ_z and u_z both vanish, and the interpretation of Ri is physically irrelevant.

An impression of the evolution of shear instability in the base case can be gained from the density field shown in Fig. 2. The figure shows that the finite-amplitude manifestation of shear instability takes the form of Kelvin-Helmholtz billows (detail shown in Fig. 3), which grow as they propagate in the downstream direction in a reference frame moving with the wave. These billows reach their full size over the downstream portion of the wave and then break down into smaller scale disturbances as they leave the wave. After the initial billows leave the wave, no further billowing is observed in the high shear region, implying that the wave becomes stable again.

For the base case, a three-dimensional simulation has also been performed. Previously, Barad and Fringer [4] studied the onset of shear instability in ISWs using three-dimensional simulations

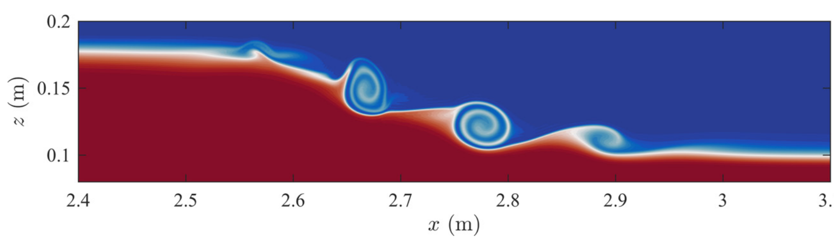

FIG. 3. Zoomed-in view of Fig. 2(b), showing detail of the billows at $t = 20$ s.

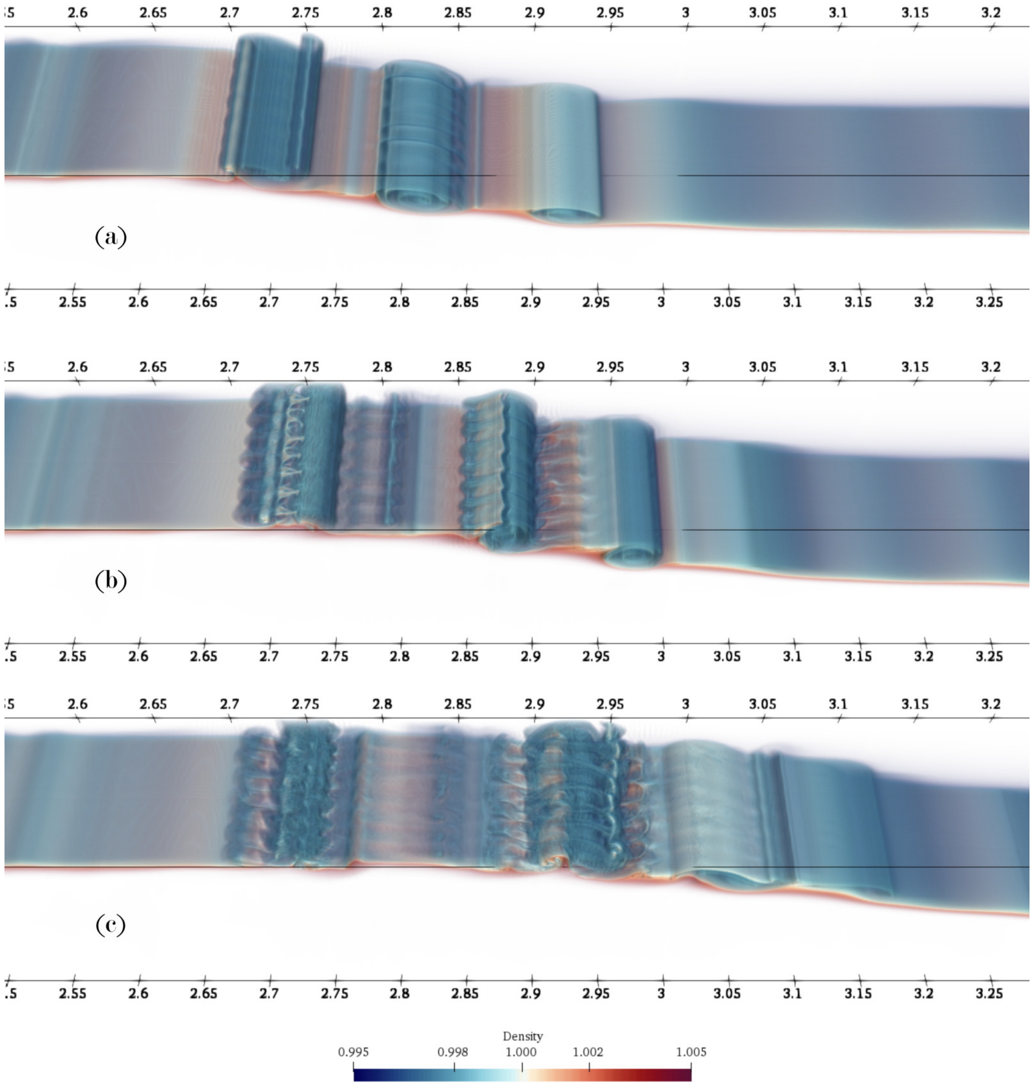

FIG. 4. Three-dimensional volume plots showing the density field in the base case at (a) $t = 22$ s, (b) $t = 24$ s, and (c) $t = 26$ s.

and showed that the primary instability remains two dimensional, even though the secondary, three-dimensional instabilities that occurred thereafter can lead to strong dissipation and mixing. Hence, they concluded that the two-dimensional approach is valid for investigating the overturns and breaking at the early stage of instability growth. In the present work, the three-dimensionalization of the flow field is visualized in Fig. 4, which shows volume plots of the density field from $t = 22$ s to 26 s. The figure shows that most billows remain two dimensional in the early stage of the onset of instability and that most of the spanwise structures in the flow field are found at the back of the wave when the billows break down into smaller-scale disturbances. This means that the onset of instability itself is unaffected by three-dimensional effects, consistent with results for the idealized case of parallel, stratified shear flow [26], as well as past studies of ISW-induced flow [4].

We note that, regardless of the model being employed, it is impossible to avoid the numerical noise and dissipation completely. This means that all numerical studies of instabilities essentially

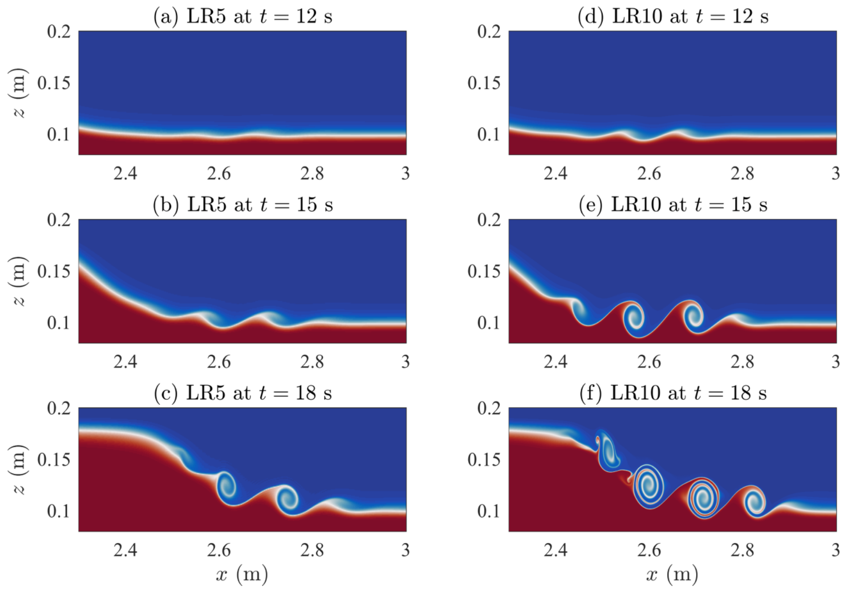

FIG. 5. Density contours showing the billow formation in the cases [(a)–(c)] LR5 and [(d)–(f)] LR10.

report a combination of their seed, the inherent instability, and their numerical dissipation. For example, Barad and Fringer [4] used an adaptive mesh refinement technique to resolve the small-scale features on the field scale, and the instabilities were excited by the numerical errors at the cell boundaries. In the present work, given the high accuracy of the spectral collocation method, the numerical model employed has less inherent numerical dissipation than most other models.

In the initial flow field, though, there are several potential sources of noise. First, as an iterative method, the algorithm used for solving the DJL equation approximates the exact solitary wave solution until a certain threshold error tolerance (10^{-4} or 0.01% of $|\eta|_{\max}$ in the present work) is reached. Second, the interpolation of the DJL solution from the coarse grid to the fine grid also introduces some noise. In fact, we have solved the DJL equation for the *large* wave to a tolerance level of 10^{-5} directly on a 8192×1024 grid and used this highly accurate solution as the initial condition without any interpolation to run the base case again on this finer grid. Nevertheless, the onset of shear instability occurs, and the results are almost identical to those shown earlier.

Finally, a third source of "noise" is the adjustment of the background state and the wave due to the diffusion of momentum (viscosity) and density (diffusivity). While the bulk parameters of ISWs such as the propagation speed and wave half-width do not change in any measurable way during this adjustment, it is possible that the more subtle features of the instability onset may be changed. This topic will be explored in detail in Sec. III C.

B. Reynolds number variations

While the assumption of inviscid fluid flows is justified in the field situation [5], viscous effects can be important on the laboratory scale. On the scale of ISW propagation, viscous adjustment alters the wave in a way such that it can develop slight asymmetry about its crest and slow down during its propagation [7], whereas on the scale of the shear layer, the presence of viscosity stabilizes the fluid flow such that the critical Richardson number at the onset of instability decreases with the Reynolds number [23].

To illustrate the Reynolds number effect on the onset of instability in the *large* wave, in Fig. 5 we compare the density fields in the cases LR5 and LR10 at three different times. The two simulations

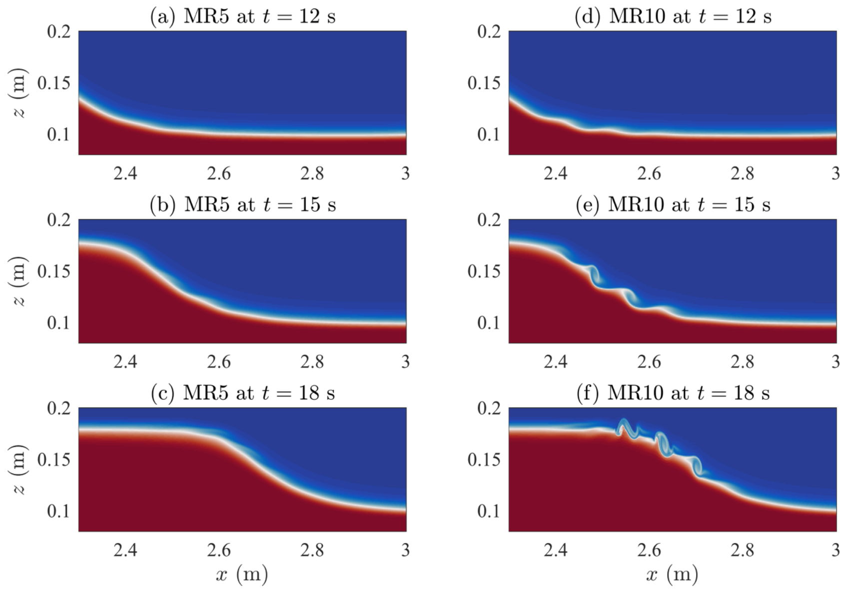

FIG. 6. Same as in Fig. 5 but for the cases [(a)–(c)] MR5 and [(d)–(f)] MR10.

are initialized from the same initial conditions, except that the case LR10 has a viscosity $\nu = 5 \times 10^{-7}$ m^2/s and a diffusivity $\kappa = 1 \times 10^{-7}$ m^2/s. It thus has a higher Reynolds number (doubled from that in LR5) but the same Schmidt number. To better resolve smaller scale features that may appear with a higher Reynolds number, the resolution of LR10 is also doubled from the case LR5 in the z directions. Figure 5 clearly shows that instability in the case LR10 grows much faster, with billows becoming fully developed at $t = 18$ s. In the mean time, secondary instabilies are also starting to develop at the edge of the billows located at $x = 2.5$ and 2.6 m.

For the *medium* wave, Fig. 6 suggests that Reynolds number becomes crucial in determining the onset of instability. This figure gives a comparison of the flow fields in the cases MR5 and MR10 at three different times. Again, by reducing the viscosity by a half, the Reynolds number in MR10 is doubled from that in MR5. The figure shows that with a higher Reynolds number, MR10 has billow formation visible at the downstream portion of the wave (though these billows have much smaller spatial dimensions), whereas with a lower Reynolds number, MR5 does not. This implies that viscous effects can limit the onset of instability. We note that for the *medium* wave the ratio $L_{\mathrm{Ri}}/L_{\mathrm{wave}}$ is slightly below the threshold $L_{\mathrm{Ri}}/L_{\mathrm{wave}} = 0.86$ [3,4]. Our results thus suggest that this criterion is not an absolute limit, but that for waves near this threshold the Reynolds number can determine the onset of instability.

Figure 7 provides a quantitative measurement of the onset of instability in the four cases discussed above by measuring the time series of the maximum vorticity. For the *large* wave, Fig. 7(a) shows that the maximum vorticity in the case LR10 is much larger than that in the case LR5. It also shows that in the case LR10, the increase of maximum vorticity starts earlier and lasts longer. For the *medium* wave, Fig. 7(b) shows that in the case MR10 there is a small instability event near $t = 20$ s, whereas in the case MR5 there is no instability at all. This is a clear indication that the onset of instability is highly dependent on the Reynolds number, since a higher Reynolds number can lead to more billowing, which is a sign of a stronger and more persistent instability.

While all of the simulations discussed above are performed on the laboratory scale, fluid flows on the field scale are typically associated with much larger Reynolds numbers. Therefore, the implication of the Reynolds number variations is that, on the field scale, spontaneous instability is in fact more likely to occur, assuming the wave is large enough.

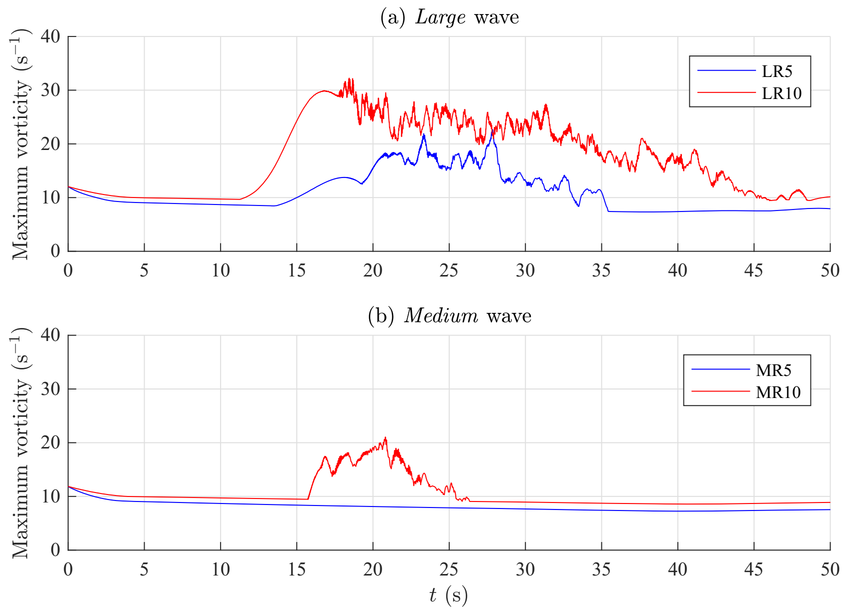

FIG. 7. Time series of the maximum vorticity of the flow fields in the cases (a) LR5 (blue) and LR10 (red) and (b) MR5 (blue) and MR10 (red).

C. Schmidt number variations

We have also studied the effect of varying the Schmidt number on what is termed "viscous" adjustment of ISWs and the onset of instability. We note that the typical Schmidt number of water is in excess of 500 when stratification is salinity controlled and roughly 7 when stratification is temperature controlled. Nevertheless, literature reporting "direct numerical simulations" often adopt a value of Sc at the order of unity [7,27,28], since the adoption of physically relevant Sc requires unattainably fine grids for resolving the sharp density interfaces. In the present work, we instead adopt a value Sc $=5$ in most simulations, except for the cases LR5S1 and LR5S20, which have Schmidt numbers Sc $=1$ and Sc $=20$, respectively. The reason for choosing this particular value is illustrated in Fig. 8. The figure shows the horizontal velocity, density, and Richardson number profiles across the *large* wave's crest at $t=0$ s and 10 s in the cases LR5S1, LR5, and LR5S20. Here the location of the wave's crest x_{crest} is determined according to the formula $x_{\text{crest}}=0.5(x_R+x_L)$, where x_R and x_L satisfy the equation $u_{\text{top}}(x_R)=u_{\text{top}}(x_L)=0.5u_{\max}$ with u_{top} being the horizontal velocity profile along the inviscid top boundary. In all of the three cases, we vary the Schmidt number by varying the diffusivity κ while keeping the viscosity ν fixed. Figure 8 shows that while the horizontal velocity at $t=10$ remains similar in all three cases, the density, and hence the Richardson number, are affected by the Schmidt number. With Sc $=1$, the Richardson number profile at $t=10$ is similar to that at $t=0$, except for a slight increase in the minimum Richardson number. With Sc $=5$ and 20, however, there is an upward shift of the location of the minimum Richardson number at $t=10$, such that the vertical structure of the Richardson number profile is different from its initial state. This indicates an offset between the centers of the shear layer and the density interface, similarly to the background state that leads to the asymmetric Holmboe instability [29]. Figure 8 thus suggests that diffusive effects play an important role in the "viscous" adjustment of ISWs and that the value Sc $=1$ is not the best choice in direct numerical simulations. Instead, higher Schmidt numbers should be adopted, and sensitivity to the Schmidt number should be tested for each phenomenon being simulated.

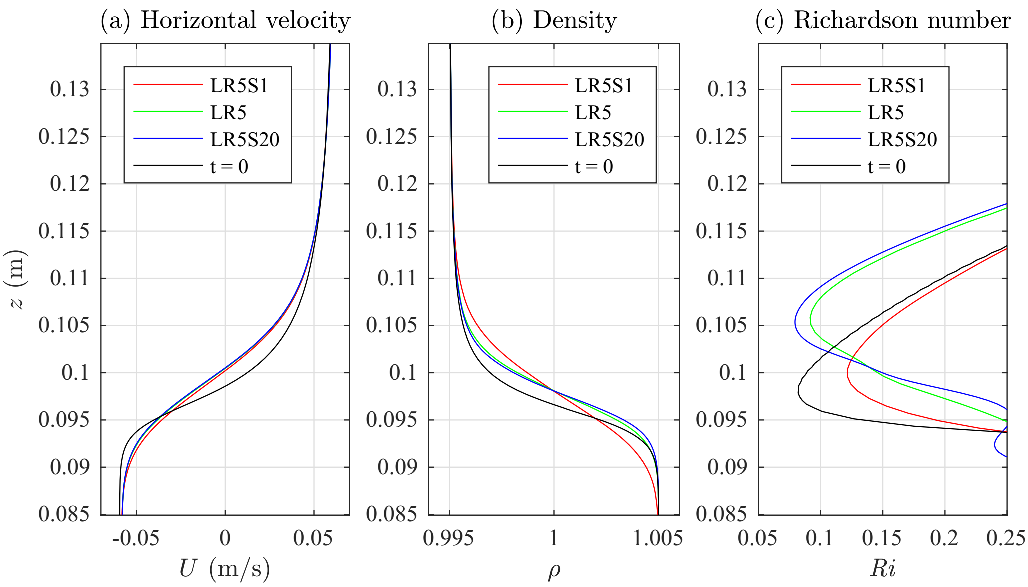

FIG. 8. Wave profiles as functions of z across the *large* wave's crest in LR5S1 (red), LR5 (green), and LR5S20 (blue) at $t = 10$ s and for the initial wave at $t = 0$ s (black).

In terms of the onset of shear instability, however, varying the Schmidt number at $\mathcal{O}(1)$ does not change the nature of primary instability fundamentally [30–32], at least for flows with a moderate-to-high Reynolds number (typically Re $\gtrsim 10^3$). The main effect of increasing the Schmidt number in shear-induced mixing includes changing the nature of secondary instabilities [33] which have a much smaller length scale than the primary instability and increasing the turbulent mixing induced by three-dimensional motions [34]. Figure 9 shows the detail of one particular billow in the cases LR5S1, LR5, and LR5S20 at $t = 20$ s. The diffusive effects can be clearly seen in this figure, particularly in Fig. 9(a), and the comparison of cases with different Schmidt numbers is similar to that shown in Fig. 2 of Rahmani *et al.* [34]. Figure 9 also shows that in all cases the billows have the same spatial structure and growth rate and that they are equally mature at this particular time. This suggests that, while the mixing efficiency of the instability is affected by the Schmidt number, the onset of instability does not depend on the Schmidt number.

D. Instability triggered by random perturbations

For the *small* wave, the cases SR5 and SR10 are not shown because no spontaneous instability is generated. Nevertheless, when velocity perturbations (in the form of additive white noise) are applied to the initial field, the wave develops an instability. Figure 10 shows the density fields of

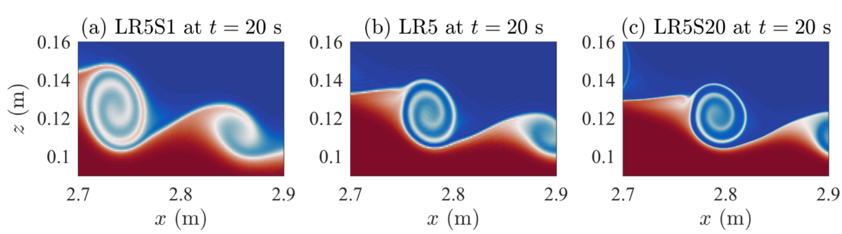

FIG. 9. Density contours showing detail of the billows in the cases (a) LR5S1, (b) LR5, and (c) LR5S20 at $t = 20$ s.

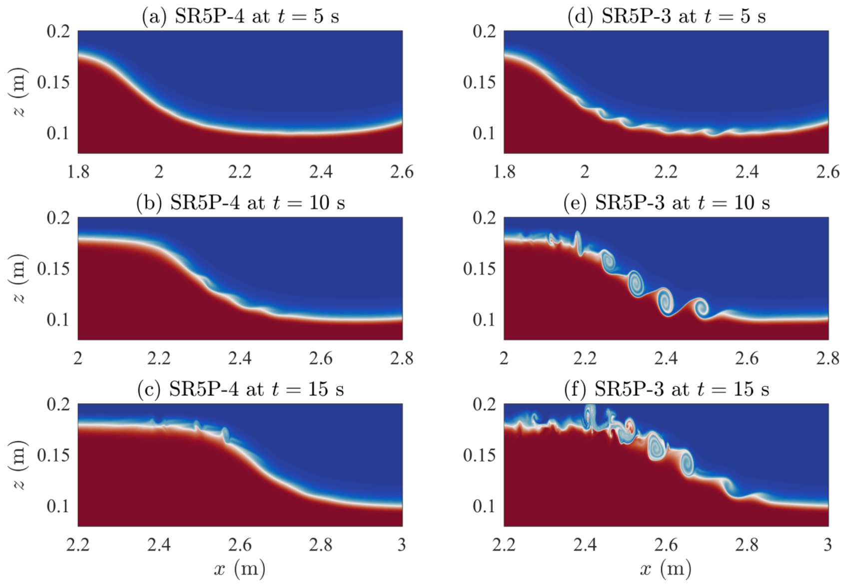

FIG. 10. Same as in Fig. 5 but for the cases [(a)–(c)] SR5P-4 and [(d)–(f)] SR5P-3. Note that we have varied the x axis for each panel in order to show the billow formation.

the cases SR5P-4 and SR5P-3 at three different times. In the case SR5P-4, velocity perturbations have an amplitude of $\epsilon = 10^{-4}$ m/s, equivalent to 0.2% of the maximum wave-induced horizontal velocity. In this case, overturning of the density field can be seen in Fig. 10(c), though none of the billows are able to develop fully before leaving the wave. On the other hand, velocity perturbations in the case SR5P-3 have an amplitude $\epsilon = 1 \times 10^{-3}$ m/s, which is an order of magnitude larger than that in SR5P-4. As a result, overturning starts at as early as $t = 5$ s. By the time $t = 15$ s, the billows have already reached their mature size and started to interact with each other. Moreover, the deformation to the pycnocline in this case also appears stronger than that in the case LR5 (shown in Fig. 2).

For the *large* wave, we further perturbed the initial velocity field in the cases LR5P-3 (with an additive white noise of amplitude 1×10^{-3} m/s), LR5P-4, and LR25P-4 (1×10^{-4} m/s). Figure 11 shows that, in addition to the Reynolds number, the formation of billows and the growth of instability also depends on the amplitude of the initial perturbations. The fastest growing instability is found in the case LR5P-3, which has billows already formed by the time $t = 6$ s. In contrast, fewer billows are formed in LR5P-4 at $t = 12$ s and in LR5 at $t = 20$ s. In the case LR25P-4, perturbations have an amplitude that is the same as those in LR5P-4, but the Reynolds number of the flow field is 5 times larger (and the resolution is also doubled in both x and z directions). Figure 11(b) suggests that this results in a much larger growth rate of the instability, such that the billowing occurs much earlier. From Figs. 11(a) and 11(b), we can also notice that in the cases LR5P-3 and LR25P-4, some of the billows are formed in front of the wave crest, whereas in the other two cases the billows are formed behind the wave crest. This result is similar to the observation of Passaggia *et al.* [7], where, by perturbing the ISWs with optimal disturbances, billow formation in front of the wave crest is also found.

We performed a linear stability analysis by extracting the background profile along the crest of the *large* wave at $t = 0$ s and using it to solve the Taylor-Goldstein equation (12) for 19 different wavelengths ranging from 0.02 to 0.2 m. The largest growth rate associated with each of these wavelengths is plotted in Fig. 12(a). The figure shows that the wavelength that yields the fastest-growing disturbances is approximately 0.06 m and that the growth rate decreases as the wavelength increases. This result agrees with our observation in Fig. 11, in the sense that the billows in the case

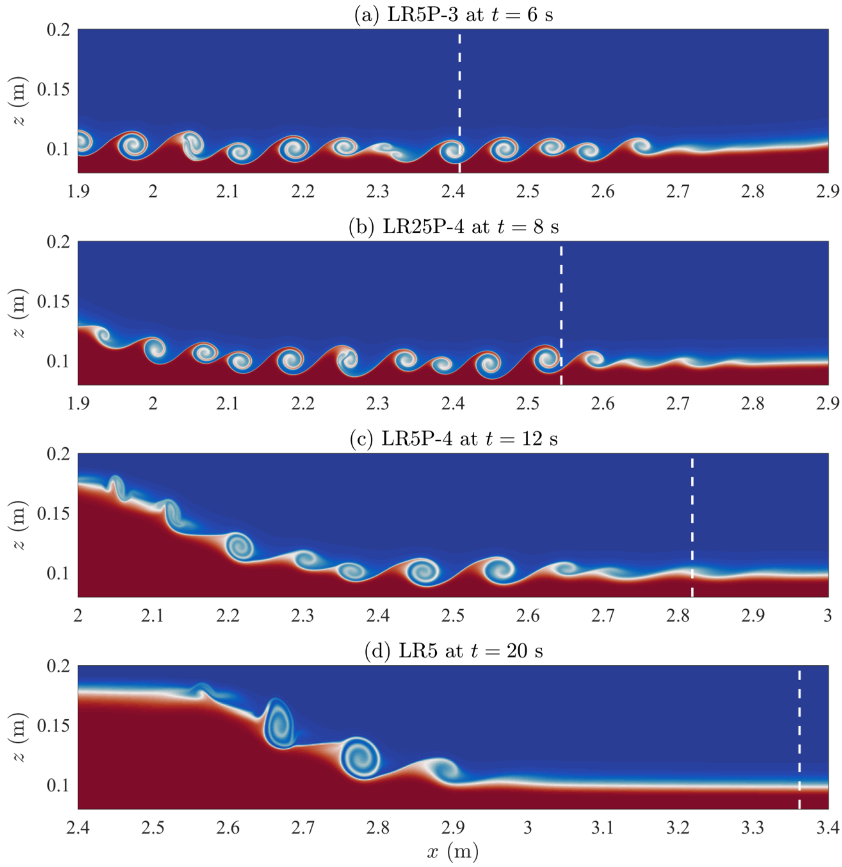

FIG. 11. Density contours showing the onset of instability in four different cases. Note that we have varied the x axis and the plot times for each panel in order to show the same maturity billows. The dashed lines indicate the locations of the wave's crest.

LR5P-3 are approximately 0.06 m apart from each other and grow fastest. In contrast, billows in the cases LR5P-4 and LR5 are farther away from each other and thus grow much slower. Therefore, the linear stability theory is able to successfully predict the growth rate of the instability from the wavelength of the disturbances.

However, the linear theory fails to explain the reason why the wavelength, and hence the growth rate, of the instability is dependent on the amplitude of the initial perturbations. To answer this question, we shall note that wave motion described by the Taylor-Goldstein equation is essentially an inviscid phenomenon, while the main effect of viscosity in a shear flow, as discussed earlier, is to stabilize the flow through diffusive type damping [23]. In particular, the strength of diffusive type damping grows as wavelength decreases. This can be visualized from the comparison of Figs. 11(b) and 11(c), which suggests that, with a smaller Reynolds number, disturbances have a larger wavelength and the instability grows slower, even though the amplitude of perturbations is the same in both cases. On the other hand, when the amplitude increases, the resulting billows become more energetic, and hence disturbances with a smaller wavelength are less likely to be damped out by the viscosity. Therefore, increasing the amplitude of the initial perturbations has a similar effect to increasing the Reynolds number of the flow field, in the sense that it allows disturbances with a smaller wavelength to manifest and thus increases the growth rate of the instability.

As a comparison, the growth rate of disturbances in a background environment extracted from the *small* wave is plotted in Fig. 12(b). This plot is very similar to Fig. 12(a), except that the growth

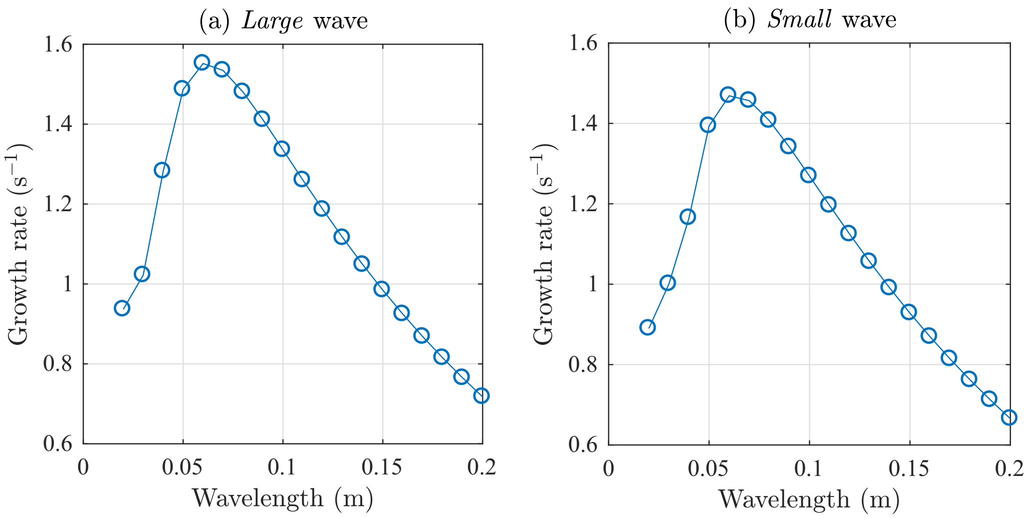

FIG. 12. Growth rate of waves of disturbance as a function of wavelength, in a background environment extracted from (a) the *large* wave and (b) the *small* wave.

rate is slightly smaller for each given wavelength. The reason for the similarity is that ISWs for this stratification are broadening limited. In other words, the density and horizontal current profiles along the waves' crests are very similar, since they both approach the so-called conjugate flow asymptotic limit [19]. The difference in the growth rate in the parallel flow theory is then due only to the small difference in the minimum Richardson numbers. However, differences in the simulations are also influenced by the much larger change in L_{Ri}, as shown in Table I. One further implication of our simulations and the linear stability analysis is that if the growth rate can be sufficiently increased, then instability can be triggered even if the ratio $L_{\mathrm{Ri}}/L_{\mathrm{wave}}$ is below the threshold value of 0.86 proposed in Fructus *et al.* [3] and Barad and Fringer [4].

E. Instability triggered by normal-mode disturbances

While the previous discussion illustrates the importance of amplitude effect in random perturbations, it does not preclude the contribution of non-normal growth [7]. In fact, it has not been determined in the previous literature if a random perturbation would also excite non-normal growth. To explore this issue, we designed a different set of experiments, labeled "SR5F-3," "LR5F-4," and "LR5F-3" in Table II. The setup of these simulations is different from that described in Sec. II but similar to that of ISW short-wave interaction in Xu and Stastna [35]. As demonstrated in Fig. 13, the overall length of the domain is extended to $L = 8$ m, with a packet of free waves, or normal modes, centered at $x = 6$ m. These waves are computed as normal modes in the linear theory, instead of

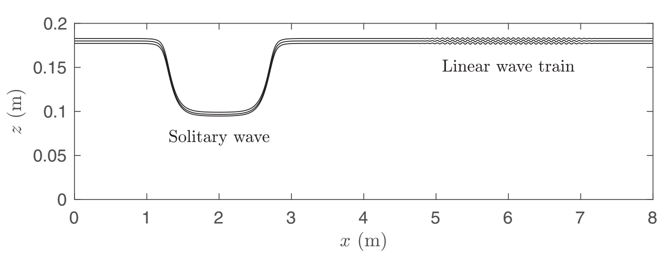

FIG. 13. Schematic diagram of the model setup for ISW-free wave interaction.

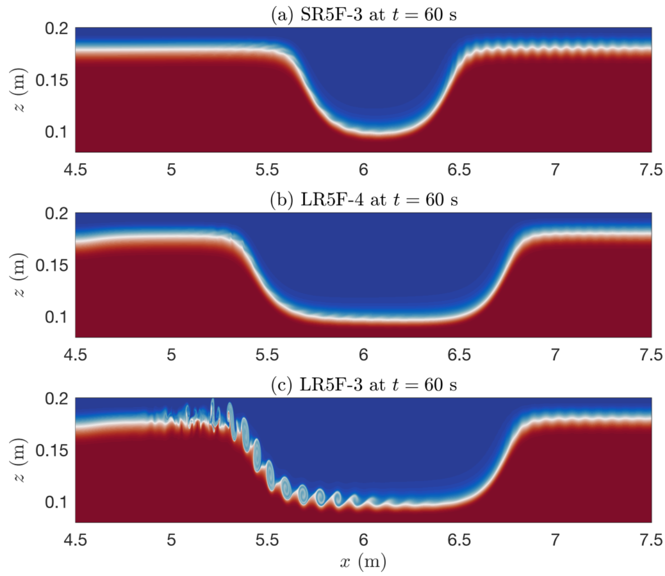

FIG. 14. Density contours showing the interaction of the ISWs with normal modes.

random perturbations. In each of these simulations, the ISW propagates to the right and interacts with the wave packet during an overtaking collision. The wavelength of these free waves is chosen to be 0.06 m, based on the results shown in Fig. 12, while the amplitude of these waves varies from 5×10^{-4} m to 2×10^{-3} m, as indicated by ϵ in Table II.

Figure 14 shows the density fields at $t = 60$ s in these three simulations. For the case SR5F-3, Fig. 14(a) shows that the *small* wave does not develop an instability when interacting with the free waves. Note that in this case the free waves have an amplitude of 2×10^{-3} m, equivalent to 1% of the total depth or 10% of the upper layer thickness. For amplitude past this range, nonlinearity is significant and the perturbations should no longer be considered a normal mode. This result is consistent with Passaggia *et al.* [7], who showed that only the optimal perturbation can grow below the threshold $L_{\mathrm{Ri}}/L_{\mathrm{wave}} = 0.86$. Since the interaction of the *small* wave with random perturbations does lead to the onset of instability (shown in Fig. 10), this suggests that random perturbations may be able to project onto the optimal perturbation to excite non-normal growth.

In the cases LR5F-4 and LR5F-3, free waves have amplitudes of 5×10^{-4} m and 1×10^{-3} m, respectively. Figure 14(b) shows that the interaction of the *large* wave with free waves that have a relatively smaller amplitude does not lead to the onset of instability, either. Figure 14(c), however, tells a different story. In this case, the onset of instability and the growth of billows can be clearly seen. This suggests that whether shear instability in ISWs can be triggered by free waves is highly dependent on the amplitude of these waves. Moreover, billows in this case are formed on the upstream side of the wave's crest. In fact, comparison to Fig. 11 shows that the instability in the *large* wave triggered by free waves is remarkably similar to that triggered by random perturbations. We note that the structure of the normal modes before the interaction (not shown here) is completely different from that of the optimal perturbation in Passaggia *et al.* [7]. Our results thus suggest that while non-normal growth is evident in random perturbations, the amplitude is a much more important factor in determining the onset of instability, whether the noise is in the form of random perturbations or normal modes.

IV. DISCUSSION AND CONCLUSIONS

In the present work, numerical simulations were performed using a spectral colocation method [10] to study the onset of shear instability in ISWs. The spectral accuracy of the numerical model combined with the high resolution adopted in the simulations guarantees that the numerical noise and numerical dissipation in the simulations is minimized. We explored the onset and growth of instability around criteria proposed in the past literature [3–5], including a minimum Richardson number $\mathrm{Ri}_{\min} < 0.1$ and a length ratio $L_{\mathrm{Ri}}/L_{\mathrm{wave}} > 0.86$. We showed that the latter is not an absolute limit, but that for waves near and below this threshold the onset of instability is also determined by the Reynolds number of the flow field and the amplitude of the external noise.

For the *large* wave ($\mathrm{Ri}_{\min} = 0.082$, $L_{\mathrm{Ri}}/L_{\mathrm{wave}} = 0.884$), the onset of shear instability occurs spontaneously (i.e., without interacting with any externally imposed physical noise). The instability takes the form of Kelvin-Helmholtz billows, which are formed behind the wave's crest and then propagate in the downstream direction in a reference frame moving with the wave. The instability remains two dimensional at the early stage of its growth, until the billows break down as they leave the downstream portion of the wave. For the *medium* wave ($\mathrm{Ri}_{\min} = 0.083$, $L_{\mathrm{Ri}}/L_{\mathrm{wave}} = 0.851$), the onset of instability is limited by viscous effects, such that the spontaneous instability is possible only when the Reynolds number is sufficiently large. For the *small* wave ($\mathrm{Ri}_{\min} = 0.085$, $L_{\mathrm{Ri}}/L_{\mathrm{wave}} = 0.801$), instability must be triggered by external perturbations of finite amplitude.

We studied the viscous and diffusive effects on the onset and growth of instability by varying the Reynolds number and the Schmidt number. We found that a larger Reynolds number leads to a stronger and more persistent instability and that near the threshold $L_{\mathrm{Ri}}/L_{\mathrm{wave}} = 0.86$, the Reynolds number can in fact determine the onset of instability. The Schmidt number, on the other hand, does not determine the onset of instability, though it can affect the mixing efficiency. Nevertheless, diffusive effects play an important role in the "viscous" adjustment of ISWs, implying that numerical studies should consider Schmidt numbers higher than the typically adopted value $\mathrm{Sc} = 1$ and that sensitivity to Schmidt number should be tested for phenomena being simulated.

We also found that the amplitude of the external noise plays an important role in triggering the instability, whether such noise is in the form of random perturbations or normal-mode disturbances. For the *small* wave, instability can be triggered by an additive white noise (but not normal-mode disturbances), even though its length ratio $L_{\mathrm{Ri}}/L_{\mathrm{wave}}$ is below the threshold 0.86. This suggests that random perturbations may be able to excite non-normal growth. For the *large* wave, further perturbing the flow field with sufficiently large perturbations leads to an instability with a much larger growth rate, such that billowing can occur in the upstream side of the wave's crest. This is observed when the externally imposed noise is in the form of normal-mode disturbances as well, implying that the importance of non-normal growth decreases as the length ratio $L_{\mathrm{Ri}}/L_{\mathrm{wave}}$ and the amplitude of perturbations increase. The results thus suggest that growth ahead of the wave crest does not require an "optimal perturbation" which may not be easily realizable in nature and that results close to the optimal transient growth discussed in Passaggia *et al.* [7] can be achieved without the full variational theory for the form of the perturbations.

Although in this paper we focused on the early stage of the instability growth, for the base case the simulation was performed for an extended period of time. The Hovmöller diagram in Fig. 15 illustrates three instability events as the wave propagates. To produce this diagram, we first computed the high-pass-filtered density field by filtering out the 15 lowest wave numbers in both x and z directions in the Fourier space at each time step. We then took the vertical averages of the high-pass-filtered density field for all time steps and combined them together into a periodic domain moving with the wave. The figure shows that, with the application of periodic boundary conditions, perturbations left behind the wave earlier in time are able to seed a new instability when interacting with the wave, allowing for the repeated onset of instability. In particular, the second instability event occurring between $t = 60$ s and $t = 100$ s is the strongest and most persistent. During this period of time, disturbances are found over the entire wave crest.

These results suggest that for large-amplitude ISWs in the field, for which the Reynolds number is expected to be high enough so that the onset of instability is not affected by it, a key component of instability onset is the amplitude of disturbances found upstream of the ISW. Indeed, given the complexity of the coastal ocean environment it is quite likely that instabilities at the field scale are

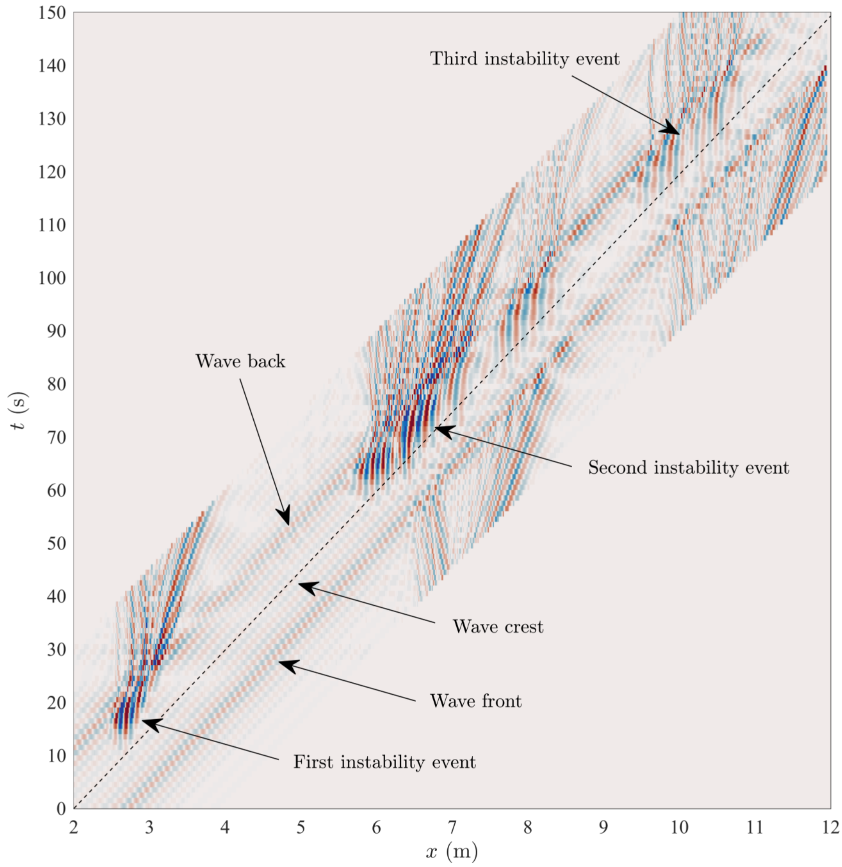

FIG. 15. Hovmöller plot of the vertically averaged, high-pass filtered density field of the base case, in a periodic domain moving with the wave. The dashed line indicates location of the wave's crest.

driven almost entirely by finite-amplitude disturbances upstream of the ISW. We note, however, that most of our results were obtained from two-dimensional simulations. While the primary instability we have studied is two dimensional, the secondary instability occurred thereafter could develop into a fully three-dimensional state, leading to strong dissipation and mixing. This means that repeated onset of instability shown in Fig. 15 could be affected by the amount of mixing that takes place due to the first instability event. For future work on this topic, three-dimensional effects should be examined in detail before any quantitative conclusions can be made.

In the present work, all waves being examined have similar properties except for the length ratio $L_{\mathrm{Ri}}/L_{\mathrm{wave}}$. Carr *et al.* [6] showed that other properties, such as wave steepness and wave amplitude, can all have a crucial influence on determining the onset of instability and the characteristics of billows. For future work on this topic, the effect of background stratification should be considered. By varying the stratification, waves of different properties (including minimum Richardson number) can be obtained. For waves that are breaking limited, the wave-induced current across the crest is not horizontally uniform [21,22], implying that criteria for the onset of instability could be more complicated. Moreover, the formation of a recirculating core and the presence of the viscous boundary layer in the case of ISWs of elevation could also affect the onset and growth of instability. The effect of a nonconstant background current could also be investigated. This is because waves in a shear background current could have a profile across their crests that is completely different from those in a zero or constant background current [13].

ACKNOWLEDGMENTS

C.X. and D.D. were supported by Queen Elizabeth II Graduate Scholarships in Science and Technology (QEII-GSST) while M.S. was supported by an NSERC Discovery Grant No. RGPIN-311844-37157. Time-dependent simulations were completed on the high-performance computer cluster Shared Hierarchical Academic Research Computing Network (SHARCNET, www.sharcnet.ca). The authors thank the two anonymous referees for their concrete suggestions that helped to improve this work.

[1] K. R. Helfrich and W. K. Melville, Long nonlinear internal waves, Annu. Rev. Fluid Mech. **38**, 395 (2006).
[2] J. N. Moum, D. M. Farmer, W. D. Smyth, L. Armi, and S. Vagle, Structure and generation of turbulence at interfaces strained by internal solitary waves propagating shoreward over the continental shelf, J. Phys. Oceanogr. **33**, 2093 (2003).
[3] D. Fructus, M. Carr, J. Grue, A. Jensen, and P. A. Davies, Shear-induced breaking of large internal solitary waves, J. Fluid Mech. **620**, 1 (2009).
[4] M. F. Barad and O. B. Fringer, Simulations of shear instabilities in interfacial gravity waves, J. Fluid Mech. **644**, 61 (2010).
[5] K. G. Lamb and D. Farmer, Instabilities in an internal solitary-like wave on the Oregon shelf, J. Phys. Oceanogr. **41**, 67 (2011).
[6] M. Carr, J. Franklin, S. E. King, P. A. Davies, J. Grue, and D. G. Dritschel, The characteristics of billows generated by internal solitary waves, J. Fluid Mech. **812**, 541 (2017).
[7] P.-Y. Passaggia, K. R. Helfrich, and B. White, Optimal transient growth in thin-interface internal solitary waves, J. Fluid Mech. **840**, 342 (2018).
[8] J. W. Miles, On the stability of heterogeneous shear flows, J. Fluid Mech. **10**, 496 (1961).
[9] L. N. Howard, Note on a paper of John W. Miles, J. Fluid Mech. **13**, 158 (1961).
[10] C. J. Subich, K. G. Lamb, and M. Stastna, Simulation of the Navier-Stokes equations in the three dimensions with a spectral collocation method, Int. J. Numer. Mech. Fluids **73**, 103 (2013).
[11] P. K. Kundu, I. M. Cohen, and D. R. Dowling, *Fluid Mechanics*, 5th ed. (Academic Press, San Diego, CA, 2012).
[12] L. N. Trefethen, *Spectral Methods in Matlab* (Society for Industrial and Applied Mathematics, Philadelphia, PA, 2000).
[13] M. Stastna and K. G. Lamb, Large fully nonlinear internal solitary waves: The effect of background current, Phys. Fluids **14**, 2987 (2002).
[14] K. G. Lamb, Extreme internal solitary waves in the ocean: Theoretical considerations, in *Proceedings of the 14th 'Aha Huliko'a Hawaiian Winter Workshop* (University of Hawaii, Honolulu, Hawaii, 2005), pp. 109–117.
[15] K. G. Lamb and L. Yan, The evolution of internal waves undular bores: Comparisons of a fully nonlinear numerical model with weakly nonlinear theory, J. Phys. Oceanogr. **26**, 2712 (1996).
[16] K. G. Lamb, Theoretical descriptions of shallow-water solitary internal waves: Comparisons with fully nonlinear waves, in *The 1998 WHOI/IOS/ONR Internal Solitary Wave Workshop: Contributed Papers*, edited by T. F. Duda and D. M. Farmer (Woods Hole Oceanographic Institution, Woods Hole, MA, 1999), pp. 209–217.
[17] M. Dunphy, C. Subich, and M. Stastna, Spectral methods for internal waves: Indistinguishable density profiles and double-humped solitary waves, Nonlin. Processes Geophys. **18**, 351 (2011).
[18] B. Turkington, A. Eydeland, and S. Wang, A computational method for solitary internal waves in a continuously stratified fluid, Stud. Appl. Math. **85**, 93 (1991).
[19] K. G. Lamb and B. Wan, Conjugate flows and flat solitary waves for a continuously stratified fluid, Phys. Fluids **10**, 2061 (1998).

[20] D. Bogucki and C. Garrett, A simple model for the shear induced decay of an internal solitary wave, J. Phys. Oceanogr. **23**, 1767 (1993).
[21] K. G. Lamb, A numerical investigation of solitary internal waves with trapped cores formed via shoaling, J. Fluid Mech. **451**, 109 (2002).
[22] K. G. Lamb, Shoaling solitary internal waves: On a criterion for the formation of waves with trapped cores, J. Fluid Mech. **478**, 81 (2003).
[23] A. Defina, S. Lanzoni, and F. M. Susin, Stability of a stratified viscous shear flow in a tilted tube, Phys. Fluids **11**, 344 (1999).
[24] W. D. Smyth, J. N. Moum, L. Li, and S. A. Thorpe, Diurnal shear instability, the descent of the surface shear layer, and the deep cycle of equatorial turbulence, J. Phys. Oceanogr. **43**, 2432 (2013).
[25] A. Maffioli and P. A. Davidson, Dynamics of stratified turbulence decaying from a high buoyancy Reynolds number, J. Fluid Mech. **786**, 210 (2016).
[26] G. P. Klaassen and W. R. Peltier, The onset of turbulence in finite-amplitude Kelvin-Helmholtz billows, J. Fluid Mech. **155**, 1 (1985).
[27] P. J. Diamessis and L. G. Redekopp, Numerical investigation of solitary internal wave-induced global instability in shallow water benthic boundary layers, J. Phys. Oceanogr. **36**, 784 (2005).
[28] S. K. Venayagamoorthy and O. B. Fringer, On the formation and propagation of nonlinear internal boluses across a shelf break, J. Fluid Mech. **577**, 137 (2007).
[29] J. R. Carpenter, G. A. Lawrence, and W. D. Smyth, Evolution and mixing of asymmetric Holmboe instabilities, J. Fluid Mech. **582**, 103 (2007).
[30] V. Birman, J. E. Martin, and E. Meiburg, The non-Boussinesq lock–exchange problem. Part 2. High-resolution simulations, J. Fluid Mech. **537**, 125 (2005).
[31] F. Necker, C. Hartel, L. Kleiser, and E. Meiburg, Mixing and dissipation in particle-driven density currents, J. Fluid Mech. **545**, 339 (2005).
[32] T. Bonometti and S. Balachandar, Effect of Schmidt number on the structure and propagation of density currents, Theor. Comput. Fluid Dyn. **22**, 341 (2008).
[33] H. Salehipour, W. R. Peltier, and A. Mashayek, Turbulent diapycnal mixing in stratified shear flows: the influence of Prandtl number on mixing efficiency and transition at high Reynolds number, J. Fluid Mech. **773**, 178 (2015).
[34] M. Rahmani, B. R. Seymour, and G. A. Lawrence, The effect of Prandtl number on mixing in low Reynolds number Kelvin-Helmholtz billows, Phys. Fluids **28**, 054107 (2016).
[35] C. Xu and M. Stastna, On the interaction of short linear internal waves with internal solitary waves, Nonlin. Processes Geophys. **25**, 1 (2018).